PNAS RESEARCH ARTICLE | MICROBIOLOGY OPEN ACCESS

SARS-CoV-2 requires acidic pH to infect cells

Alex J. B. Kreutzberger[a,b], Anwesha Sanyal[a,b], Anand Saminathan[a,b], Louis-Marie Bloyet[c], Spencer Stumpf[c], Zhuoming Liu[c], Ravi Ojha[d], Markku T. Patjas[e], Ahmed Geneid[e], Gustavo Scanavachi[a,b], Catherine A. Doyle[f], Elliott Somerville[b], Ricardo Bango Da Cunha Correia[a,b], Giuseppe Di Caprio[b,g], Sanna Toppila-Salmi[h], Antti Mäkitie[e], Volker Kiessling[i,j], Olli Vapalahti[d,k,l], Sean P. J. Whelan[c,1], Giuseppe Balistreri[d,k,m,1], and Tom Kirchhausen[a,b,g,1]

Edited by Peter Palese, Icahn School of Medicine at Mount Sinai, New York, NY; received June 07, 2022; accepted August 03, 2022

Severe acute respiratory syndrome coronavirus 2 (SARS-CoV-2) cell entry starts with membrane attachment and ends with spike (S) protein–catalyzed membrane fusion depending on two cleavage steps, namely, one usually by furin in producing cells and the second by TMPRSS2 on target cells. Endosomal cathepsins can carry out both. Using real-time three-dimensional single-virion tracking, we show that fusion and genome penetration require virion exposure to an acidic milieu of pH 6.2 to 6.8, even when furin and TMPRSS2 cleavages have occurred. We detect the sequential steps of S1-fragment dissociation, fusion, and content release from the cell surface in TMPRRS2-overexpressing cells only when exposed to acidic pH. We define a key role of an acidic environment for successful infection, found in endosomal compartments and at the surface of TMPRSS2-expressing cells in the acidic milieu of the nasal cavity.

SARS-CoV-2 | live-cell imaging | virus entry | 3D imaging | infection route

Severe acute respiratory syndrome coronavirus 2 (SARS-CoV-2) cell entry begins with engagement at the cell surface and ends with deposition of the viral contents into the cytosol by membrane fusion. The first step is binding of the viral spike (S) protein with its cellular receptor angiotensin converting enzyme (ACE2) (1–4). The last step delivers the viral genomic RNA in association with the nucleocapsid protein (N), which is removed for translation of the input genome (5, 6). Proteolytic activation of S by additional host-cell factors is necessary for it to function as a fusogen. Cleavage of S by furin in producer cells (7) generates the S1 receptor binding subunit noncovalently associated with the S2 fusion subunit. The S protein is cleaved by cell surface or endosomal proteases during virion entry into host cells, which activate the viral fusion machinery (1, 8–10). This entry-associated proteolysis of S has led to the current model of two routes of infectious cell entry, as follows: fusion of viral and cellular membranes at the host-cell surface or fusion following endosomal uptake (6).

The cellular proteases that are involved in processing S during entry include the transmembrane serine proteases TMPRSS2 or TMPRSS4 found at the cell surface (1, 8) and the endosomal cathepsins that require the acidic milieu of the compartments in which they are enriched (1, 10). Processing of S by TMPRSS proteases or by cathepsins, at a site designated S2', depends on prior cleavage at the furin site in the producer cells (7, 11, 12). TMPRSS cleavage has been thought to result in infection from the plasma membrane and cathepsin cleavage, in cells lacking TMPRSS activity, with infection from endosomes (5, 6). Chemical inhibitors of TMPRSS or cathepsin proteases in cells in culture indeed show that infection of some cell types is more sensitive to inhibition of endosomal cathepsins, whereas others are more sensitive to inhibition of TMPRSS proteases (1, 9). TMPRSS inhibitors such as camostat and nafamostat are in clinical development as SARS-CoV-2 therapeutics, further highlighting the need to understand how entry pathways depend upon specific proteases.

To analyze the routes of cellular uptake that lead to successful fusion and release of virion contents into the cytoplasm, we developed a set of tools that allow direct visual tracking of the uptake of single virions and release of their contents. Using a chimeric vesicular stomatitis virus (VSV) in which SARS-CoV-2 S has replaced the endogenous glycoprotein gene (G), we modified the virus to permit the separate tracking of the S protein and the viral contents. We engineered a structural component of the replicative core of VSV, the phosphoprotein (P), to append to its amino terminus enhanced green fluorescent protein (eGFP), for tracking the virion content. This eGFP-P chimeric virus is structurally fluorescent and depends upon S for entry. We also sparsely labeled the S protein by direct conjugation with a fluorescent dye, allowing us to visualize the steps of entry, from S1 fragment release to membrane fusion, including virion content release into cells during productive infection. We have found that content

Significance

Infection by SARS-CoV-2 depends upon the large spike (S) protein decorating the virions and is responsible for receptor engagement and subsequent fusion of viral and cellular membranes allowing release of virion contents into the cell. Using new single-particle imaging tools to visualize and track the successive steps from virion attachment to fusion, combined with chemical and genetic perturbations of the cells, we provide direct evidence for the cellular uptake routes of productive infection in multiple cell types and their dependence on proteolysis of S by cell surface or endosomal proteases. We show that fusion and content release always require the acidic environment from endosomes, preceded by liberation of the S1 fragment which depends on angiotensin converting enzyme receptor engagement.

Author contributions: A.J.B.K., S.P.J.W., G.B., and T.K. designed research; A.J.B.K., A. Sanyal, A. Saminathan, R.O., M.T.P., A.G., G.S., E.S., R.B.D.C.C., S.T.-S., A.M., O.V., and G.B. performed research; A.J.B.K., A. Saminathan, L.-M.B., S.S., Z.L., C.A.D., G.D.C, V.K., and S.P.J.W. contributed new reagents/analytic tools; A.J.B.K., V.K., and T.K. analyzed data; A.J.B.K. and T.K. wrote the paper; and S.P.J.W. oversaw the work to generate and characterize the VSV chimeras, participated in early discussions, and helped edit portions of the manuscript.

Competing interest statement: T.K. is a member of the Medical Advisory Board of AI Therapeutics, Inc.

This article is a PNAS Direct Submission.

[1]To whom correspondence may be addressed. Email: kirchhausen@crystal.harvard.edu, giuseppe.balistreri@helsinki.fi or spjwhelan@wustl.edu.

This article contains supporting information online at http://www.pnas.org/lookup/suppl/doi:10.1073/pnas.2209514119/-/DCSupplemental.

Published September 1, 2022.

release requires acidic pH and that it occurs principally from endosomes irrespective of the cell type and irrespective of the dependence of the virus on TMPRSS2 or cathepsin-mediated processing of S. Only mild acidification of the medium allows efficient entry at the plasma membrane. We correlate our findings with studies of infection by several human isolates of SARS-CoV-2.

Results

Cell Entry of Individual Virions Mediated by SARS-CoV-2 S. We used live-cell fluorescence microscopy to monitor the uptake of single VSV-SARS-CoV-2 virions that depend upon SARS-CoV-2 S for infection (Wuhan Hu-1 isolate and Delta and Omicron variants, chimeras generated as described; *Materials and Methods* and ref. 13) and for the Wuhan variant also containing a fluorescent internal structural protein, P, fused at its amino terminus to eGFP (eGFP-P) (*SI Appendix*, Fig. S1). We counted the number of tagged particles internalized at 1 h postinoculation at a multiplicity of infection (MOI) of 0.5 and found 50 to 70 particles in Caco-2, Calu-3, and Vero cells, but about three times that number in Vero-TMPRSS2 cells, which overexpress TMPRSS2 (*SI Appendix*, Fig. S1 *D* and *E*), presumably because of more efficient TMPRSS2 cleavage in the high expression cell line. Examination of the labeled virions by spinning-disk confocal microscopy showed distinct, diffraction-limited puncta with a single, Gaussian distribution of fluorescent intensities (*SI Appendix*, Fig. S2*A*), consistent with the presence of single virus particles and the absence of virion aggregates. We also labeled the S protein sparsely with the fluorescent dye Atto565 NHS ester (25 to 35 dyes per virion), with a minimal effect on particle infectivity (*SI Appendix*, Fig. S2 *A–D*). The double labeling allowed us to track the viral S protein separately from the virion contents.

SARS-CoV-2 S-Mediated Entry Requires Endocytosis. We used live-cell volumetric, lattice-light-sheet fluorescence microscopy (LLSM) (14) to obtain three-dimensional (3D) views of virion cell entry over time during their uptake into cells (Fig. 1 *A–E*; *SI Appendix*, Fig. S3 and Movie S1). We incubated cells for 8 min, transferred them to the LLSM, and recorded sequential 3D stacks from a single cell, acquiring a full stack every 2 s, for 10 min (300 stacks total). We then moved quickly to an adjacent cell and recorded a similar 10-min series of 300 stacks, after which we moved finally to a third neighboring cell, for 10 min. The sequence of representative 10-plane projections in Fig. 1*B* shows that particles attached to the cell surface during the initial 8-min incubation, followed by efficient internalization at later time points. The figure shows images from Vero-TMPRSS2 cells; we obtained similar results for Vero, Caco-2, and Calu-3 cells, as shown in *SI Appendix*, Fig. S3. The views from 20 and 30 min postinoculation also showed many examples of intracellular spots labeled with eGFP-P only, representing delivery of the VSV ribonucleoprotein core (RNP) into cells visualized as the separation of fluorescent eGFP-P from the membrane-bound, Atto565-labeled S glycoprotein.

We confirmed that the views in Fig. 1*B* reflected the outcome of sequential internalization and RNP delivery events by tracking individual particles in the volumetric time series acquired using LLSM (Fig. 1*C*). Single virions attached to cells during the 8-min period following the addition of virus, and ~90% (1,508/1,692) of the attached particles had internalized during the 30-min time course, as recorded in 60 time-lapse 3D videos from 20 cells. The representative 10-plane projection in Fig. 1*C* obtained during the initial 10-min interval shows several single-particle examples of virion internalization and three events of RNP core release (for similar results with Vero, Caco-2, and Calu-3 cells, see *SI Appendix*, Fig. S3). The highlighted example in Fig. 1*C* and the complete ortho projection in Fig. 1*D* show a fluorescent spot corresponding to a virus particle, which was first captured at the cell surface, then undergoing rapid directed movement toward the cell interior, due to endocytosis and intracellular traffic of virus-containing vesicles. Dissociation of the eGFP-P from the Atto565 signals marks delivery of the genome into the cytosol (*SI Appendix*, Figs. S3–S7). In a total of 60 Caco-2, Calu-3, Vero, and Vero-TMPRSS2 cells, we detected a separation of signals at an intracellular location for 138/1,692 trajectories during the 30-min interval starting 2 min after an initial 8-min inoculation (Fig. 1*E*) and only one dissociation event at the cell surface (for a Vero-TMPRSS2 cell). The remaining virions remained associated with endosomal membranes (see below). The fluorescent signals from eGFP-P released in these time frames remained stable and punctate in the cytosol during the duration of the 10-min acquisition, and any released eGFP-P in the cytosol at the outset of the second or third 10-min time series remained stable for the entire 10-min recording. Moreover, we never observed uncoated (delivered) particles (i.e., released eGFP-P) in the early frames of the time lapse from the first cell. These observations rule out the possibility of rapid, early entry events from the cell surface or from endosomes during the "blind" 8 min during inoculation, and we conclude that an endocytic route accounted for all but one of the detected VSV-SARS-CoV-2 fusion events in these experiments.

An analysis of mean square displacement (MSD) curves from 3D, single-particle trajectories allowed us to determine the dynamic regime of the particle at any time point after attachment. The alpha coefficient (α) in the anomalous diffusion equation ($<r^2> = 6Dt^{\alpha}$) corresponds to confined motion ($\alpha < 0.8$) for the virus attached to the cell surface, directed motion ($\alpha > 1.2$) for intracellular particles with colocalized Atto565-labeled S and eGFP-P-labeled RNP, presumably associated with endosomes, and Brownian motion ($0.8 < \alpha < 1.2$) for eGFP-P spots diffusing in the cytosol. The results shown in Fig. 1*F* (which corresponds to the viral particle traced in Fig. 1 *C* and *D*) and the summary for all tracked particles in Fig. 1*G* (*SI Appendix*, Figs. S3–S7) illustrate the moment at which an RNP escapes into the cytosol ($\alpha = 1.07$), while the tagged S remains associated with an endosome ($\alpha = 1.93$, see below). The remaining particles, representing nonproductive events, remained attached to endosomes (Fig. 1*G*).

The chimeric VSV particles are roughly 80 by 200 nm (15, 16) and appear in the microscope as diffraction-limited spots. Endosomes typically range in diameter from 300 to 1,000 nm (17). Thus, a subset of fluorescent endosomes are larger than the diffraction limit, facilitating the use of an increased apparent size of an Atto565 fluorescent spot as a proxy for viral membrane fusion with the surrounding (larger) endosomal membrane (*SI Appendix*, Fig. S8*A*). Using this approach, we detected fusion in 17 ± 4% ($n = 20$ virions), 28 ± 2% ($n = 61$ virions), 23 ± 2% ($n = 27$ virions), and 27 ± 6% ($n = 30$ virions) of the traces in Vero, Vero-TMPRSS2, Caco-2, or Calu-3 cells, respectively. All the events coincided with release into the cytosol of the eGFP-P-labeled RNP core of VSV (Fig. 1*E* and *SI Appendix*, Figs. S3 and S7). We did not observe a release of the virion contents at the plasma membrane (Fig. 1*E* and *SI Appendix*, Figs. S3–S7), indicating that S-mediated infection of cells only occurred through an endocytic pathway.

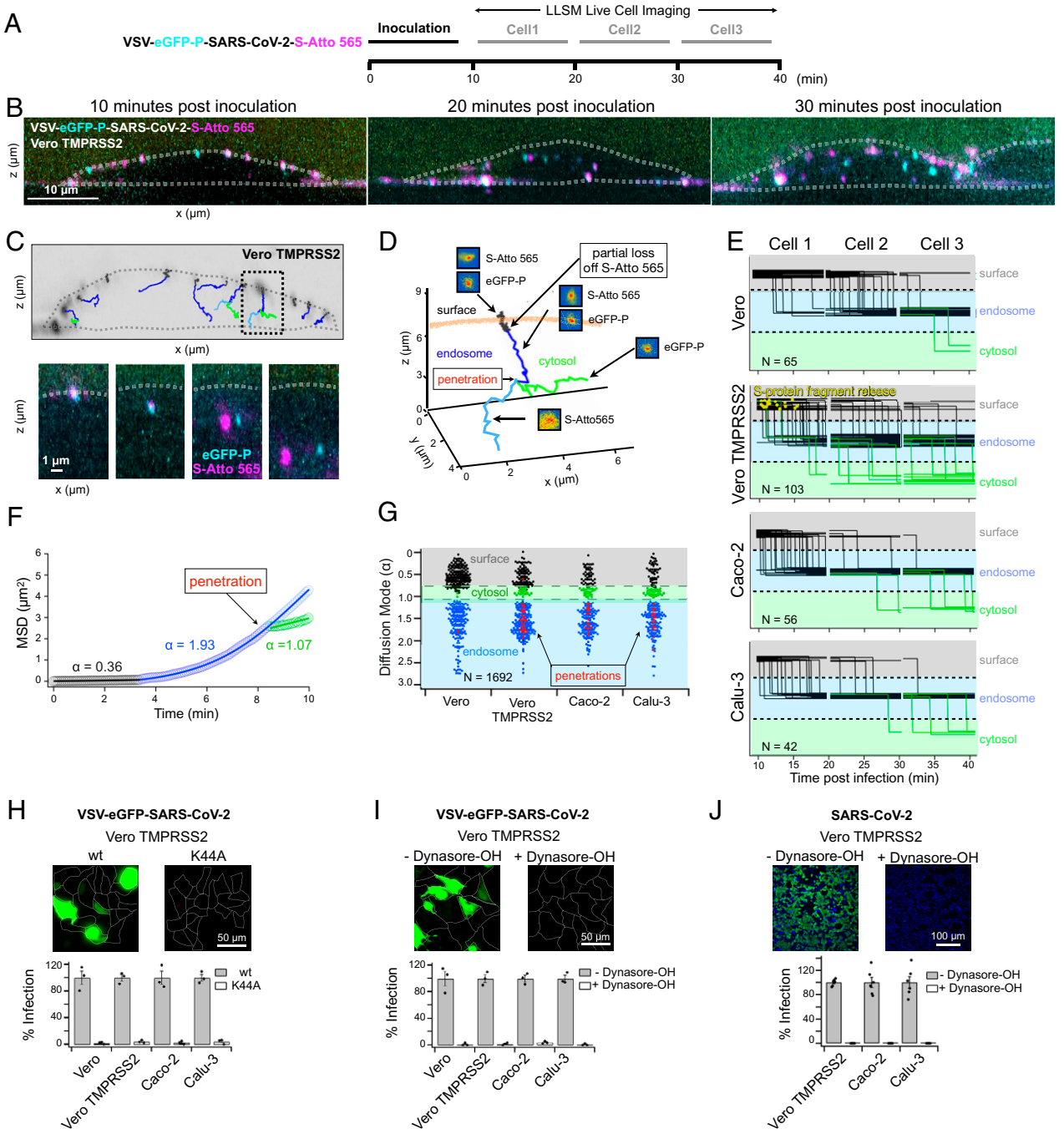

Fig. 1. SARS-CoV-2 infection requires endocytosis. (*A*) Schematic of live-cell volumetric LLSM imaging experiments (*B*–*G*) used to obtain 3D time series of VSV-eGFP-P-SARS-CoV-2-S-Atto 565 entry into Vero TMPRSS2 cells during early stages of infection using an MOI of 2. For each experiment, three cells were consecutively imaged volumetrically every 4.7 s for 10 min. (*B*) Maximum intensity projections showing fluorescently tagged VSV-SARS-CoV-2 within 1 μm in thickness optical sections from the first frame of the time series acquired for representative cells 1, 2, and 3. (*C*) Representative single-virion trajectories of VSV-eGFP-P-SARS-CoV-2-S-Atto 565 within a 1-μm optical slice of a time series acquired during the first 10-min of cell 1. Traces highlight particles at the cell surface (black) and within the cell volume after endocytosis (blue), in both cases containing colocalized eGFP-P and S-Atto 565; it also shows traces in the cytosol (green) containing eGFP-P upon its separation from the Atto565 signal (light blue). Single images highlighting these events are shown in the panels below. (*D*) Orthogonal projection of the traced event highlighted in *C*. (*E*) Representative summary of 266 virion traces analyzed during cell entry. Data from single coverslips (out of five) obtained per each cell type are shown. Vertical traces highlight the transfer of virions from the cell surface to the cell interior (assumed to be in endosomes because the colocalization of the eGFP-P with S-Atto 565 signals) or from endosomes to the cytosol (upon loss of colocalization of the eGFP-P and S-Atto 565 signals). Events corresponding to a step-wise loss of the S-Atto 565 signal at the cell surface are indicated (yellow). (*F*) Representative plot illustrating the MSD for the trajectory depicted in *D* when the particle is at the cell surface (black), in endosomes (blue), or in the cytosol upon separation of eGFP-P in the cytosol (green) from S-Atto565 that remains in endosomes (light blue). (*G*) Summary dot plot showing the diffusion mode (α) for 1,692 virion trajectories and corresponding 139 penetration events; all penetration events occurred from endosomes except for 1 event at the cell surface in a single Vero TMRSS2 cell. The plot highlights the confined motion ($\alpha < 0.80$) of virions at the cell surface, trajected motion ($\alpha > 1.2$) in endosomes, and Brownian motion ($0.80 < \alpha < 1.2$) in the cytosol. (*H*–*J*) Effect of inhibition of endocytosis in the infection by VSV-eGFP-SARS-CoV-2 (*H* and *I*) or a human isolate of SARS-CoV-2 (*J*). *Top* panel shows examples of infection observed in representative fields of Vero TMPRSS2 overexpressing or not the dominant-negative dynamin K44A mutant or treated or not with 40 μM dynasore-OH. Images in the *Top* panels were obtained using spinning-disk confocal microscopy and show maximum intensity projections. Results from similar infections obtained with different cell types are shown in the *Bottom* panel. The difference of results between control conditions and inhibition of endocytosis by K44A dynamin overexpression or incubation with dynasore-OH incubation was statistically significant with a *P* value of <0.001 using an unpaired *t* test.

SARS-CoV-2 S-Mediated Infection Requires Endocytosis. Dynamin, a large GTPase required for cargo uptake in clathrin-mediated or fast endophilin-mediated endocytosis (18), is susceptible to interference by a dominant negative mutant, K44A (19). To test whether dynamin-dependent endocytosis is necessary for SARS-CoV-2 S–mediated infection, we transiently over expressed the dominant-negative mutant in Caco-2, Calu-3, Vero, and Vero-TMPRSS2 cells. We monitored the effect on infection of these cells by VSV-SARS-CoV-2 that expresses eGFP as a marker of infection (VSV-eGFP-SARS-CoV-2) according to the scheme summarized in *SI Appendix*, Fig. S9*A*, and we quantified infection by single-cell imaging at 8 h postinoculation. In control cells, to achieve comparable infectivity, we used 10 times more VSV-SARS-CoV-2 for Caco-2 and Calu-3 cells than for Vero or Vero-TMPRSS2 overexpressing TPMRSS2 (*SI Appendix*, Fig. S9 *B* and *C*). Irrespective of the cell type, infection was inhibited by the dominant-negative dynamin mutant (Fig. 1*H*) or by addition of dynasore-OH, a small-molecule dynamin inhibitor (20) (Fig. 1*I*). Dynasore-OH addition at 1 h postinoculation had no effect on viral infectivity, consistent with inhibition of an early, entry-related event, but not with later inhibition of viral gene expression (*SI Appendix*, Fig. S9*C*). We previously reported that S-mediated infection of cells by VSV-SARS-CoV-2 correlates well with infection by SARS-CoV-2 (9, 13, 21, 22). In accord with that correlation, dynasore-OH also inhibited infection of Calu-3 and Vero-TMPRSS2 cells by a SARS-CoV-2 Wuhan (B.1) clinical isolate (Fig. 1*J*). These results show a critical role for endocytosis in SARS-CoV-2 infection of multiple cell types in culture including cells that express TMPRSS2.

Viral Entry from Endosomes. Our data show that internalized virus particles reached internal membrane compartment(s) from which fusion and genome entry into the cytosol occurred. To establish the identity of the(se) endosomal compartments, we used live-cell LLSM to track particles entering SVG-A cells ectopically expressing ACE2, or both ACE2 and TMPRSS2, and gene edited for fluorescent labeling of specific endosomal compartments. (Fig. 2*A* and *SI Appendix*, Fig. S10). Single-particle tracking of 6,815 viruses over a 50-min period starting from 30 min postinoculation of cells revealed VSV-SARS-CoV-2 particles trafficked from the cell surface to early endosomes marked with early endosomal antigen 1 fused to the fluorescent protein Scarlett (EEA1-mScarlet) and subsequently to late endosomes/lysosomes marked with a Halo-tagged version of the cholesterol transporter Niemann Pick C1 NPC1-Halo-JFX646 (examples for single virions shown in Fig. 2 *B* and *C* and *SI Appendix*, Figs. S11 and S12). We only detected particles located in the interior localizing with the endosomal markers in early frames of the time lapse from the first cell taken at the end of the 30-min inoculation period. Like with the other cells, these observations also rule out for SVG-A cells the possibility of entry events from the cell surface or from endosomes during the 30-min inoculation period.

To establish the location of the compartments from which the virion contents were released, we identified the point at which the trajectory of the eGFP-P signal changed from directed ($\alpha > 1.2$) to Brownian ($0.8 < \alpha < 1.2$) concomitant with a loss of colocalization with endosomal markers (examples for single virions shown in Fig. 2 *D* and *E* and *SI Appendix*, Figs. S13 and S14). All entry events occurred from compartments marked with either EEA1 or NPC1 in cells expressing TMPRSS2 and only from NPC1 compartments in cells lacking TMPRSS2 (Fig. 2*F* and *SI Appendix*, Fig. S15).

Release of S1 at the Surface of Cells Expressing TMPRSS2. Membrane fusion mediated by S depends on its proteolytic cleavage and dissociation of the S1 fragment (6). Cleavage alone does not release S1; the required trigger is ACE2 binding (*SI Appendix*, Fig. S19). The addition of soluble ACE2 ectodomain to VSV-SARS-CoV-2 particles activated by trypsin, to bypass TMPRSS2, released about 70% of the Atto 565 label, providing a reasonable estimate for the relative fractions of S1 and S2 (*SI Appendix*, Fig. S19 *A–D*). In live-cell imaging experiments with TMPRSS2-expressing cells, we noted a partial loss of Atto 565 intensity from labeled VSV-SARS-CoV-2 particles after they attached to the cell surface (*SI Appendix*, Fig. S16). In these experiments, we used a microfluidics device to introduce the virus to cells while in the LLSM, enabling us to detect attachment directly. We interpreted the loss of Atto 565 signal as S1 dissociation, and we took it as a proxy for cleavage by TMPRSS2 at the S2' site on an ACE2-attached S protein since it was only observed in cells expressing TMPRSS2. Dissociated S1 will remain attached to ACE2 for some time, and in about ~2% of the events, we could indeed detect lateral spreading (interpreted as diffusion in the plasma membrane) associated with the abrupt partial reduction of the punctate Atto 565 signal. We found ~25% loss of the Atto 565 signal per particle in ~78% of particles at the surface of Vero-TMPRSS2 cells expressing TMPRSS2 (Fig. 3 *A–D*) within the first 10 min of LLSM single-particle tracking (Fig. 1*E*). In all cases, the loss was in a single step with a half time of 2 s or less (Fig. 3*B* and *SI Appendix*, Fig. S16). The signal reduction, which preceded endocytosis, was never associated with RNP delivery (e.g., eGFP-P) from the cell surface (Fig. 1 *E*, cell 1), except under the special circumstances of slightly acidic medium during inoculation, as described in the following section (Figs. 3 *E–J* and 4). The signal loss at the cell surface depended strictly on TMPRSS2 activity, as it was inhibited by 10 μM Camostat and was absent in Vero cells lacking TMPRSS2 (Fig. 3*D*). The decrease in punctate intensity, which we interpret as the release of S1, occurred in less than 5% of particles attached to Caco-2 or Calu-3 cells, which naturally express TMPRSS2 (Fig. 3*D*). This result suggests that in these cells, cleavage at S2' by TMPRSS2 occurs primarily after uptake into endosomes.

Viral Membrane Fusion Requires Acidic pH. Endosomes undergo rapid acidification, and acidic pH is a trigger that induces fusogenic conformational changes in many viral envelope proteins. We therefore examined the effect of pH on productive viral entry by adjusting the pH of the medium at 10 min postinoculation. From 187 traces from Vero-TMPRSS2 cells incubated at pH 6.8, we observed 84 fusion events at the cell surface, as defined by the loss of Atto 565 signal and by accompanying eGFP-P delivery into the cytosol (Fig. 3 *E–H* and *SI Appendix*, Fig. S17). The abrupt partial loss of punctate signal, interpreted as S1-fragment release, always preceded fusion (signaled by diffusion in the plasma membrane of the remaining Atto 565 signal with a half-life of about 20 s) and by eGFP-P delivery into the cytosol, typically within 10 s (Fig. 3 *E* and *F*). The assignment as membrane fusion was confirmed by showing the temporal overlap between the S-Atto 565 diffusion from the viral particle into the plasma membrane with the dequenching followed by plasma membrane diffusion of Cy5-DOPE used to label the viral membrane (*SI Appendix*, Fig. S8*B*). We defined eGFP-P delivery into the cytosol by a change in its motion from confined ($\alpha < 0.8$) when on the cell surface to Brownian ($0.8 < \alpha < 1.2$) when in the cytosol (Fig. 3*G*). In the absence of S1 release, we did not detect S-Atto 655 diffusion or eGFP-

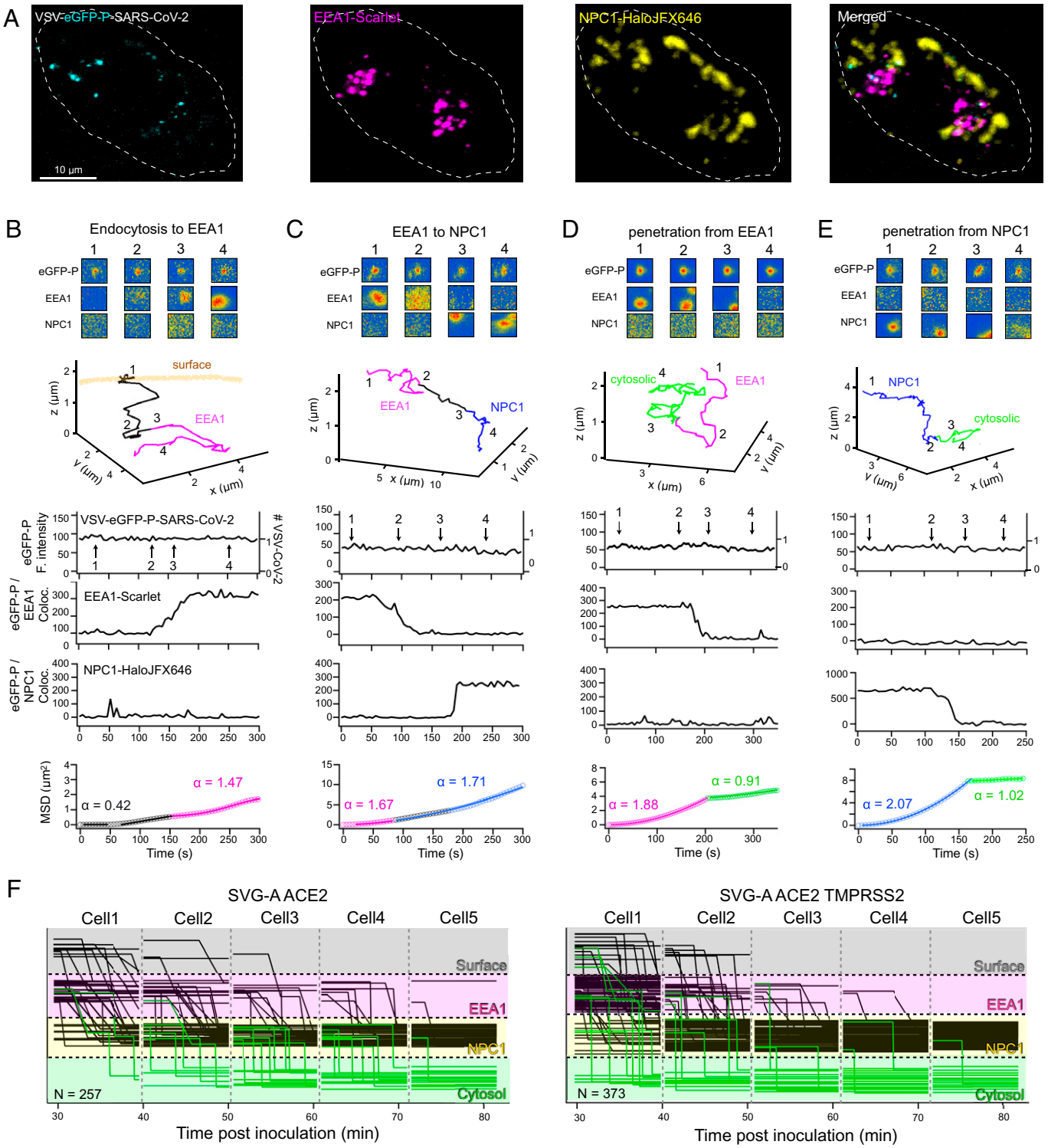

Fig. 2. Endocytic entry routes of VSV-SARS-CoV-2. VSV-eGFP-P-SARS-CoV-2 was used to infect SVG-A gene edited to express early endosomal antigen 1 fused to the fluorescent protein Scarlet (EEA1-Scarlet) as an early endosomal marker and for late endosomal/lysosomal compartments a Halo-tagged version of the cholesterol transporter Niemann Pick C1 (NPC1-Halo) together with ectopic expression of ACE2 and TMPRSS2 and volumetrically imaged using LLSM according to Fig. 1. (*A*) Representative 2-µm projection from the first frame of the time series acquired 8 min after inoculation. (*B–E*) Representative examples of single trajectories of VSV-eGFP-P-SARS-CoV-2 highlighting the extent of colocalization between eGFP-P and EEA1 or between eGFP-P and NPC-1 Halo labeled with JFX646 (*Top* panel), the orthogonal projection of the trajectory (*Middle* panel), and corresponding plots for the number of VSV particles on the spot and extent of colocalizations and MSD (*Bottom* panels). Additional examples are found in related *SI Appendix*, Figs. S11–S16. (*F*) Representative summary of results for 257 and 373 virion traces analyzed during cell entry from single coverslips (out of a total of five) plated with SVG-A ACE2 or SVG-A ACE2 TMPRSS2. Vertical and diagonal traces highlight the transfer of virions from the cell surface to its interior and associated with early or late endosomes/lysosomes as defined by colocalization of eGFP-P with EEA1-Scarlet or eGFP-P with NPC1-Halo, respectively.

P delivery into the cytosol. We conclude that the release of S1 and subsequent or concomitant exposure to acidic pH result in the release of virion contents into the cell.

Incubation of Vero-TMPRSS2 cells at pH 6.2 rather than 6.8 during inoculation prevented the release of the S1 fragment and hence prevented viral fusion at the cell surface (Fig. 3 *E*, *G*, and *H*).

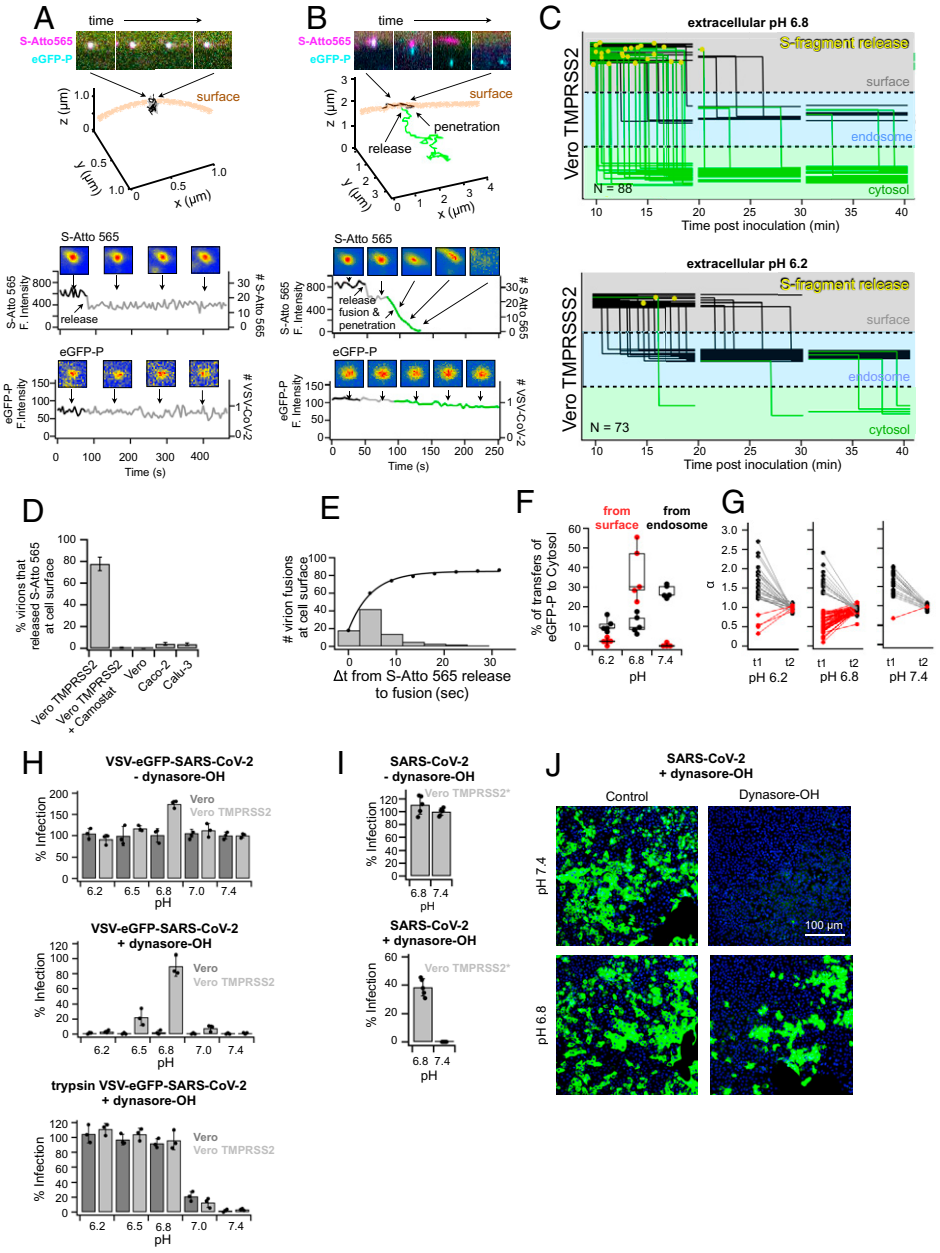

Fig. 3. Surface entry route of SARS-CoV-2. (*A*–*G*) VSV-eGFP-P-SARS-CoV-2-S-Atto 565 was used to infect Vero TMPRSS2 cells and used to study the effect by acidic pH in the medium on the TMPRSS2-mediated surface release of the S-fragment, on the cellular location of fusion and genome delivery and on infectivity. (*A* and *B*) Single-virion trajectories of VSV-eGFP-P-SARS-CoV-2-Atto565 in a Vero TMPRSS2 cell incubated at pH 6.8 showing in *A* an example of S-release at the surface without subsequent fusion and in *B* an example of S-release followed by penetration of eGFP-P to the cytosol. Orthogonal views of the tracings and corresponding time-dependent fluorescent intensities for S-Atto 565 and eGFP-P are shown. (*C*) Representative summary from 237 virion traces analyzed during cell entry. Data from single coverslips (out of 5) obtained per each pH condition in the medium are shown. Vertical traces of cells incubated at 6.8 highlight the efficient transfer of virions from the cell surface to the cell interior (based on loss of signal colocalization between eGFP-P and S-Atto 565 and corresponding change of diffusion from constrained to directed). Events of stepwise partial loss of S-Atto 565 are indicated (yellow). Similar data with cells incubated at pH 6.2 show an accumulation of virions in endosomes, complete absence of fusion events from the cell surface, and limited number of fusion events from endosomes. (*D*) Data showing the fraction of virions that released the S-fragment from virions at the cell surface of Vero TMPRSS2 cells incubated at pH 6.8 in the absence or presence of 10 μM Camostat or of Vero E6, Caco-2, or Calu-3 cells also at pH 6.8 and in the absence of Camostat. The difference of results between control and all other conditions was statistically significant with a *P* value of <0.0001 using an unpaired *t* test. (*E*) Cumulative plot corresponding to the dwell time between the stepwise partial drop of the S-Atto 565 signal of a virion at the cell surface and fusion defined by surface spreading of the remaining Atto 565 signal and transfer into the cytosol of eGFP-P. Data from 86 traces and from 5 experiments. (*F*) Effect of extracellular pH on the transfer of eGFP-P of virions from the cell surface (red) or from endosomes (black) to the cytosol. Each dot represents average ± SD from 5 coverslips with 3 cells imaged per coverslip and at least 600 virus tracked per condition. The line across each box represents the median of distribution, and the *Top* and *Bottom* lines represent the quartiles. (*G*) Effect of extracellular pH of the cell medium on the mode of diffusion of the eGFP-P signal associated with a virion before and after delivery from the surface (red) or from endosomes (black) to the cytosol. (*H*) pH bypass infection experiments to test the effect of extracellular acidic pH on the extent of infection of Vero or Vero TMPRSS2 cells by VSV-eGFP-SARS-CoV-2 alone or treated for 30 min with 1 μg/mL trypsin; experiments carried in the absence (*Top* panel) or presence (*Middle* and *Bottom* panels) of 40 μM dynasore-OH. Each data point represents an experiment. In each case, the values determined at pH 6.8 and 7.4 are significantly different with a *P* value of at least <0.0003 using an unpaired *t* test. (*I*) pH bypass infection experiment using authentic SARS-CoV-2 and Vero TMPRSS2* cells in the absence or presence of 40 μM dynasore-OH. Each data point represents an experiment. No statistical difference was observed in the absence of dynasore-OH between pH 6.8 and pH 7.4 ($P = 0.13$); the difference was statistically significant in the presence of dynasore-OH ($P < 0.0001$) using an unpaired *t* test. (*J*) Representative immunofluorescence images showing the effect of dynasore-OH on the infection by authentic SARS-CoV-2 of Vero TMPRSS2* cells at different pHs used to generate the data shown in *I*. The extent of infection determined by immunofluorescence (green) with an antibody specific for the N protein of SARS-CoV-2 and nuclear staining (blue) with DAPI is shown.

This pH dependence is consistent with an expected loss of TMPRSS2 proteolytic activity as the pH falls below 6.5. When cells were incubated at pH 7.4 throughout infection, we did not observe any particle fusion and content release at the cell surface, even though TMPRSS2 cleavage, as detected by S1-fragment release, still occurred (Fig. 3 *E*, *G*, and *H*).

The efficiency of entry by VSV-SARS-CoV-2 tracked by visualizing content release or by extent of infection increased in Vero-TMPRSS2 cells at pH 6.8 (Fig. 3*H*). To investigate further the requirement of acidic pH for efficient SARS-CoV-2 S-mediated membrane fusion, we carried out bypass experiments to initiate infection directly at the cell surface. We blocked endocytic uptake into cells with dynasore-OH and exposed bound particles to different pH ranging from 6.2 to 7.4. Infection of Vero, Caco-2 or Calu-3 cells was blocked regardless of the pH, whereas Vero cells overexpressing TMPRSS2 were readily infected by acid triggering of the S protein at the cell surface (Fig. 3*J* and *SI Appendix*, Fig. S18).

These results were consistent with the observed lack of release of the S1-fragment from viruses at the surface of Vero, Caco-2, or Calu-3 cells (Fig. 3*D*). To eliminate a requirement for TMPRSS2 cleavage of S, we preactivated particles by incubation with trypsin before inoculating the cells. These preactivated particles were as infectious in Vero TMPRSS2 cells treated with dynasore-OH and inoculated at a pH < 7 as non-trypsinized particles in the same cells and conditions. Thus, trypsin and TMPRSS2 cleavages were equally effective in activating the particles. With progressive acidification of the medium, infection increased, reaching a maximum at pH 6.6 and remaining constant to pH 6.2 (Fig. 3*H*). These results show that S-mediated fusion requires pH < 7. We obtained similar results concerning the effect of pH on infectivity of authentic SARS-CoV-2 with cells in which endocytosis was blocked and genome penetration depended solely on cell-surface fusion events (Fig. 3 *I* and *J*).

Influence of S Protein Variation on Infectious Entry Pathways. We found that response to infection inhibitors and the requirement for endocytosis and proteolytic cleavage of S for the VSV chimera with the Delta variant S protein were essentially the same for the chimera with the S protein from the original Wuhan-Hu1 isolate (Fig. 4 *A–D* and *SI Appendix*, Figs. S20 and S21). Conserved events included release of the S1 fragment from receptor-bound virions attached to Vero-TMPRSS2 cells (Fig. 4*B*), and S1-fragment release followed by fusion and genome penetration when inoculation was at pH 6.5 to 6.8 (Fig. 4*C*). Both Wuhan-Hu1 and Delta also showed enhanced infectivity of Vero-TMPRSS2 cells inoculated at pH 6.8 (Fig. 3*H* and Fig. 4 *A–D*).

Examination of the entry pathway mediated by the S protein of Omicron varied with the cell type used to produce the virus. VSV-Omicron produced in Vero-TMPRSS2 cells depended on TMPRSS2 activation for the infection of Vero-TMPRSS2, although somewhat fewer virions released the S1 fragment at the cell surface (Fig. 4 *B–D*). VSV-SARS-CoV-2 chimeras with Omicron S produced in MA104 cells could not be activated by TMPRSS2 and failed to infect or fuse from the surface of Vero-TMPRSS2 cells at pH 6.8 (Fig. 4 *A–D* and *SI Appendix*, Figs. S20 and S21). Infection required activation by cathepsins for fusion and infection from endosomes (Fig. 4 *A–D* and *SI Appendix*, Figs. S20 and S21). Trypsin treatment of VSV-SARS-CoV-2-Omicron, which cleaves at both the furin and TMPRSS protease sites (23), allowed infection to proceed from the cell surface at acidic pH, independent of the producer cell line, even in the presence of an endocytosis inhibitor (Fig. 4 *A–D* and *SI Appendix*, Figs. S20 and S21).

Sequence analysis of the genomic RNA from the VSV-SARS-CoV-2 chimeric viruses confirmed the presence of the TMPRSS2 and furin cleavage sites in Omicron S. As furin cleavage in producing cells is essential for subsequent proteolysis by TMPRSS2 in the infecting cell, we tested whether incomplete furin cleavage explained the differential susceptibility to TMPRSS2 activation. We found much less cleavage of the Omicron S for virus produced in MA104 cells (Fig. 4*D*) than for virus produced in Vero-TMPRSS2 cells (Fig. 4*D*). Particles with furin-cleaved S were susceptible to TMPRSS2 activation (Fig. 4 *A–D*), released the S1 fragment (Fig. 4*A*), and fused at pH 6.8 (Fig. 4 *B* and *D*).

Intranasal pH. Our results suggest that an acidic environment is required for successful infection, found in endosomal compartments and at the surface of TMPRSS2-expressing cells purposely exposed to mildly acidic extracellular pH conditions. Since the expression of TMPRSS2 appears to be highly expressed in a subset of cells located in the nasopharyngeal cavity (24, 25), we asked whether this milieu would be acidic. Using a pH catheter placed in the left and right nasal cavities of 17 healthy male and female volunteers, we found a mildly acidic pH of around 6.6 (Fig. 4*E*), which is in agreement with earlier measurements (26, 27).

Discussion

We examined how SARS-CoV-2 Wuhan and its variants Delta and Omicron enter host cells using a combination of high-resolution live-cell 3D imaging and quantitative assays for viral infectivity. Real-time tracking of single VSV-SARS-CoV-2 chimeric particles by LLSM allowed us to visualize directly, with a sensitivity and time resolution substantially greater than any previous work, the key early steps of viral infection, as follows: virion binding, release of the S1 fragment upon cleavage by TMPRSS2, viral membrane fusion, and genome penetration into the cytosol. These observations revealed a previously unsuspected requirement to fuse by exposure to pH between 6.5 and 6.8, even after priming by TMPRSS2 and the attendant release of S1 and the S2' fragment (Fig. 5).

The current understanding, derived in part from earlier work on SARS-CoV, has assumed that the only requirement for low pH was for cathepsin L activity when TMPRSS2 was absent or for furin cleavage during exit from the producing cell, a prerequisite for TMPRSS2 digestion (1, 11, 12, 28–30). Our results instead distinguish three complementary routes of productive entry, of which all involve exposure of the entering particle to pH < 6.8. The two principal routes are by uptake and traffic to early endosomes, for TMPRSS2-primed virions, or to late endosomal compartments, for cathepsin cleavage in cells regardless of the presence or absence of TMPRSS2. A third, minor route does not require virion uptake but instead proceeds entirely at the cell surface, but only if cell attachment is at a pH range between 6.5 and 6.8. These observations define the alternative, multistep pathways of SARS-CoV-2 entry and restrict the conditions for cell-surface penetration.

The released Atto 565-labeled fragment diffused laterally in the membrane, away from the labeled virion, consistent with our identification of the fragment as S1, which we expect to remain attached to ACE2. The release, which always preceded membrane fusion, was independent of exposure to acidic pH. Its dissociation was necessary but not sufficient for S2 to undergo

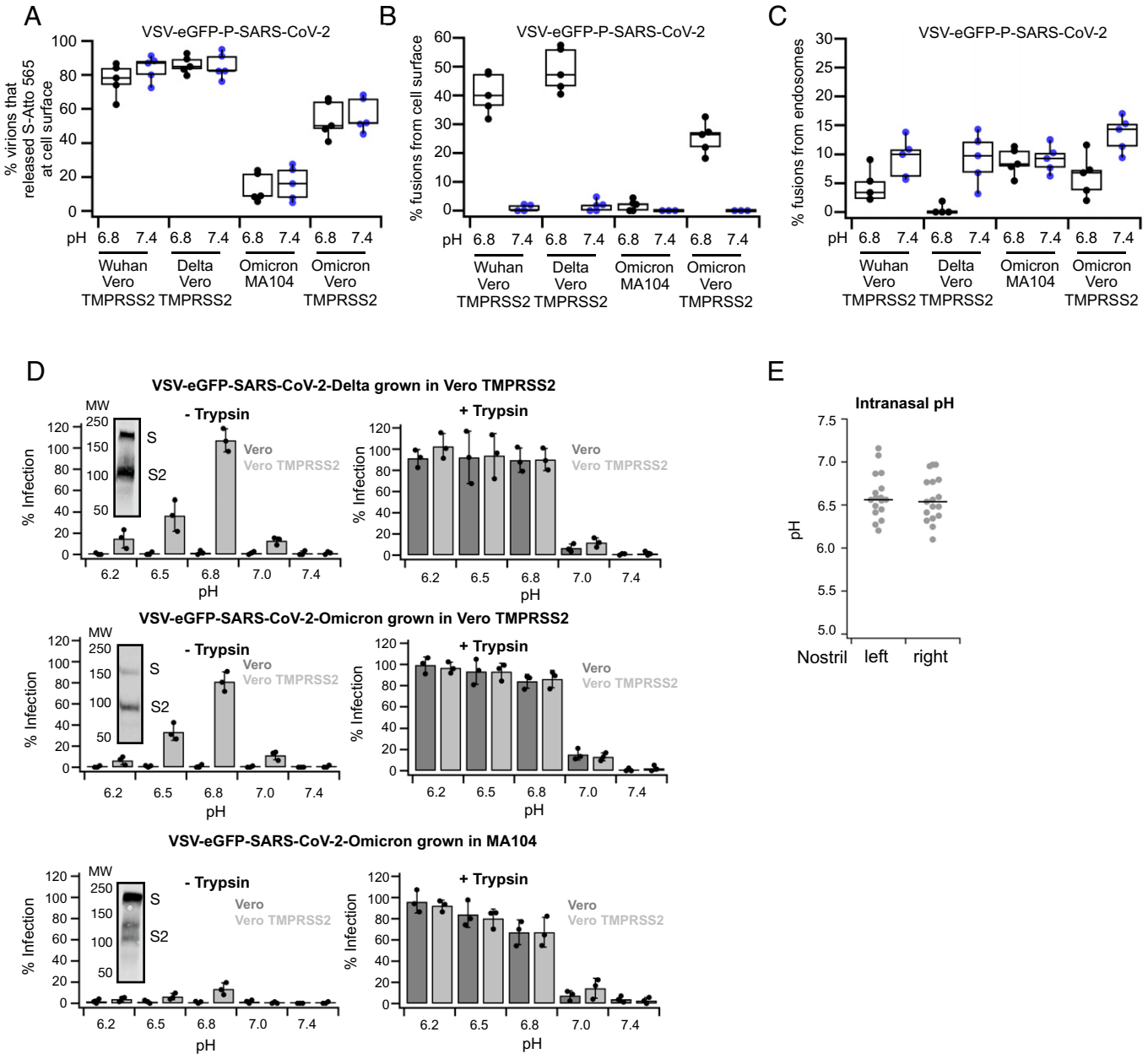

Fig. 4. Entry routes of VSV-SARS-CoV-2 variants are conserved. (*A*–*C*) Effect of extracellular pH and type of cells infected with the indicated variants of VSV-eGFP-P-SARS-CoV-2 on (*A*) the extent of S-fragment release from the cell surface and of (*B*) fusion from the cell surface or (*C*) from endosomes. (*D*) Experiments to determine the effect of extracellular pH on the extent of infection by the Delta and Omicron variants of VSV-SARS-CoV-2 in the presence of 40 μM dynasore-OH. The pH bypass experiments in the *Right* panel were done with trypsin-cleaved virions. The *Bottom* two rows compare results obtained with the Omicron variant grown in MA104 or Vero TMPRSS2 cells. Western blot shows cleavage states of the S protein of VSV-SARS-CoV-2-Omicron grown in different cell types. The bypass pH experiments in the *Left* panels show statistical differences between pH 6.8 and pH 7.4 ($P < 0.0001$) for Delta and Omicron grown in Vero TMPRSS2 and of minimal significance for Omicron grown MA 104 using an unpaired *t* test. Similar analyses for the experiments in the *Right* panels show statistical differences between pH 6.8 and pH 7.4 for Delta ($P < 0.0001$) and for Omicron grown in Vero TMPRSS2 ($P < 0.0001$) or MA 104 ($P = 0.0015$). (*E*) Nasal pH values determined from 17 healthy individuals. Each dot represents a single pH determination by the pH catheter at the lower turbinate of the right and left nostrils.

its full, fusion-promoting conformational change. Release required S2' site cleavage, as evidenced by its absence in the presence of the TMPRSS2 inhibitor Camostat and by its absence, even in TMPRSS2-expressing cells, at pH lower than about 6.5, where TMPRSS2 is inactive. Trypsin cleavage in our experiments circumvented TMPRSS2 activity, and we indeed observed entry and infection at pH as low as 6.2.

The structure of the S and the distribution of lysine residues suggest that about 70% of the Atto 565 label will be on S1 and, hence, from the fraction of total label released, that about 25% of the S-protein trimers will have shed the S1 fragment upon the interaction with membrane-bound ACE2, assuming that dissociation of the 3 S1 fragments is cooperative. We estimate from the ratios of stained band intensities on sodium dodecyl-sulfate polyacrylamide gel electrophoresis that the VSV chimeras have 15 to 20 S trimers on their surface, and we infer from these numbers that, on average, 3 to 4 S proteins will have lost S1, liberating their S2 fragments to extend and interact with the host-cell membrane. This estimate is consistent with the likely fraction of the virion surface that makes contact with the cell membrane and with the dependence of S1 shedding from a trimer on its binding to ACE2. It is also consistent

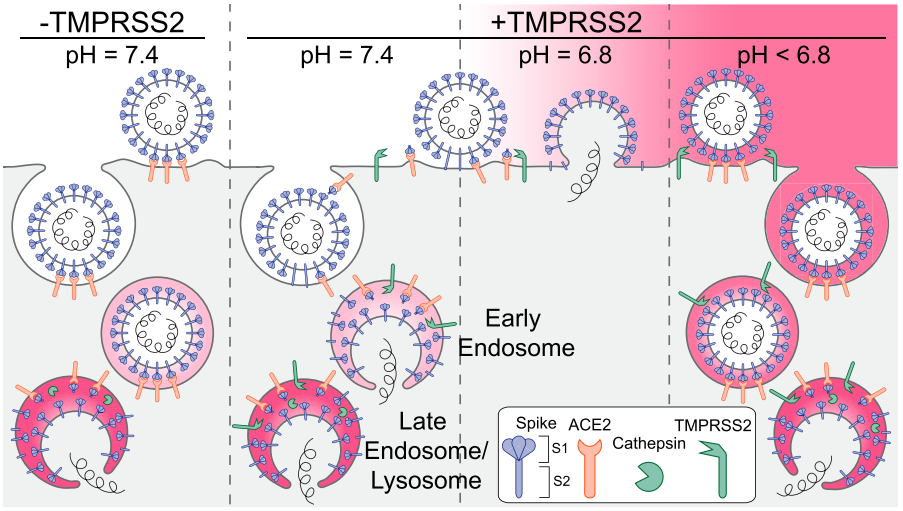

Fig. 5. Schematic representation of the principal entry routes SARS-CoV-2 uses for infection. Entry starts with membrane attachment and ends with S protein–catalyzed membrane fusion releasing the viral contents into the cytosol. Fusion activity depends on two proteolytic cleavage steps, namely, one typically carried out by furin in the producing cell and the second by TMPRSS2 on the cell surface on in endosomes of the target cell. Alternatively, endosomal cathepsins can carry out both cleavages. Exposure of the virus to an acidic milieu is essential for membrane fusion, genome penetration, and productive infection. Fusion and penetration occur only in acidic early and late endosomal/lysosomal compartments but not at the cell surface, even when the furin and TMPRSS2 cleavages have both occurred. Fusion and penetration can occur at the cell surface of cells expressing TMPRSS2 if the extracellular pH is ~6.8.

with the number of active fusion proteins on other viruses, including VSV itself, required for fusion to proceed (31–34).

Syncytium formation between cells expressing SARS-CoV-2 S and cells expressing ACE2, often used as a S-mediated fusion assay, does not appear to depend upon acidic pH. But the interface between the two cells will have vastly more S than the interface between a virus and a target cell. Thus, even a low probability of fusion events at neutral pH should be sufficient to create a fusion pore, which can widen and spread across the entire cell–cell junction.

Release of the S1 fragment from a S also detaches that S from ACE2. Because cleavage at the S2' site was complete in our experiments, any S bound by ACE2 would probably have released the S1 fragment. Continued association with the host cell would thus have depended on formation of alternative contacts as S1 dissociates. We propose that formation of an extended intermediate and insertion of the S2 fusion peptides into the host-cell membrane creates the interactions that retain the virion at the cell surface. This proposal further implies that protonation of one or more S2 residues at acidic pH then enables S2 to collapse toward the folded-back, postfusion trimer of hairpins and pull together the viral and host-cell lipid bilayers.

The Omicron variant is more refractory to furin cleavage than previously isolated strains. Its entry pathway will thus depend on the level of furin activity in the producing cells. We indeed found that when grown in Vero-TMPRSS2 cells, Omicron VSV chimeras were susceptible to S2' cleavage by TMPRSS2 and entered from early endosomes or at the cell surface at mildly acidic pH, but when grown in MA104 cells, they required cathepsin cleavage in late endosomes for entry. With authentic SARS-CoV-2 virus, TMPRSS2 susceptibility similarly depended on the cells in which the virus was propagated. These observations resolve some ambiguities in the literature concerning the role of TMPRSS2 in Omicron infection (35–37).

Together with differential protease activities, the pH of respiratory mucosa could also influence viral tropism. The pH of the airway-facing surface of the nasal cavity is between 6.2 and 6.8 (our observations and ref. 26). Thus, in principle, rapid entry could occur at the surface of TMPRSS2-expressing cells in the nose. In other parts of the nasopharyngeal cavity and in the lung, the pH is neutral (38), and we would not expect virus to fuse in those tissues until its endocytic uptake.

Our suggestion that at neutral pH, a relatively long-lived, extended S2 intermediate may be present at the virus–cell interface bears both on potential therapeutic interventions and on the availability of otherwise occluded epitopes to mucosal antibodies. The persistence of an extended intermediate after gp120 release during HIV entry is thought to account for inhibition of viral infectivity by the peptide fusion inhibitor entfuvirtide and for neutralization by antibodies that recognize epitopes unavailable on a prefusion Env trimer. Our results are consistent with observations that comparable interventions can impede SARS-CoV-2 infection in animal models (39).

Materials and Methods

Materials and Cells. All materials and cells used in this study are described in detail in *SI Appendix*.

Generation of VSV-SARS-CoV-2 Chimeras. The generation of a replication-competent recombinant VSV chimera expressing eGFP where the glycoprotein G was replaced with S protein Wuhan-Hu-1 strain (VSV-eGFP-SARS-CoV-2) has been described (13). Additional details for the generation of the VSV recombinants expressing eGFP and SARS-CoV-2 S variants for Delta (B.1.617.2) and Omicron (B.1.1.529) are described in *SI Appendix*.

Generation of SVG-A Cells Expressing ACE2 and TMPRSS2. SVG-A cells ectopically expressing ACE2 and TMPRSS2 were generated by lentivirus transduction. Briefly, lentiviruses encoding human ACE2 or TMPRSS2 were generated as follows: HEK293T packaging cells were seeded at 3.8×10^6 cells in a 10-cm tissue culture plate and grown in complete Dulbecco's modified Eagle medium (DMEM) supplemented with 10% vol/vol fetal bovine serum (FBS) at 37 °C and 5% CO_2.

Transfection mixtures containing 90 μL Lipofectamine 3000 (Thermo Scientific L3000001), 1 μL psPAX2 (1.3 pmol; Addgene #12260), 0.6 μL pMD2.G (0.72 pmol; Addgene #12259) and 1.2 μL TMPRSS2/pLX304 or ACE2/pLJM1 (1.64 pmol; gifts from Sean Whelan), in 5 mL OptiMEM medium (Thermo Scientific 31985062) were mixed by pipetting and incubated for 20 min at room temperature. A total of 0.7 million cells were plated in a 10-cm plate 18 h prior to transfection; the medium was then replaced with the entire transfection mixture and cells were incubated for 6 h at 37 °C, after which the medium was replaced with 15 mL complete DMEM. After 12 h, this medium was replaced

with 15 mL of complete DMEM, which was then harvested 24 h later after further growth. After the addition of another 15 mL of medium, cells and virus were allowed to grow, ending with a second harvest of medium. The medium was cleared of debris by centrifugation at 5,000 × g for 5 mins at room temperature and supernatants containing lentivirus stored at −80 °C.

Ectopic stable expression of ACE2 and TMPRSS2 was achieved by transduction of SVG-A cells (gift from Walter J. Atwood, Brown University) gene edited to simultaneously express fluorescently tagged early and late endosomal markers EEA1 and NPC1 fused to mScarlet or Halo, respectively (21). Briefly, SVG-A 1×10^6 cells were seeded in a well from a 6-well plate and grown overnight in minimum essential medium (MEM) with 10% FBS. Cleared medium containing ACE2 or TMPRSS2 lentivirus (1 mL) was added to the cells and incubated for 16 h, following replacement with fresh medium cells that were incubated for an additional 24 h. Cells were allowed to grow for another 4 d in the presence of 7 μg/mL puromycin to select for ACE2-expressing cells or 5 μg/mL blasticidin for TMPRSS2-expressing cells. Surviving cells were grown in the absence of puromycin or blasticidin for 4 d, and cell stocks were frozen and kept in liquid nitrogen. SVG-A cells simultaneously stably expressing ACE2 and TMPRSS2 were obtained by transduction with lentivirus encoding TMPRSS2 and selection with blasticidin of cells stably expressing ACE2.

Preparation of VSV Chimeras for Imaging and Infection Experiments. All VSV-SARS-CoV-2 variants were grown in MA104 cells in 15 to 20 150-mm dishes and infected at a MOI of 0.01 as previously described (9, 13); in addition, the Omicron variant was also grown in Vero TMPRSS2 cells. Briefly, media containing the viruses were collected 72 h postinfection and clarified by centrifugation at 1,000 × g for 10 min at 4 °C. A pellet with virus and extracellular particles was obtained by centrifugation in a Ti45 fixed-angle rotor at 72,000 × g (25,000 rpm) for 2 h at 4 °C and then resuspended overnight in 0.5 mL PBS at 4 °C. This solution was layered on top of a 15% sucrose-PBS solution, and a pellet with virions was obtained by centrifugation in a SW55 swinging-bucket rotor at 148,000 × g (35,000 rpm) for 2 h at 4 °C. The resulting pellet was resuspended overnight in 0.4 mL PBS at 4 °C, layered on top of a 15 to 45% sucrose-PBS linear gradient, and subjected to centrifugation in a SW55 swinging-bucket rotor at 194,000 × g (40,000 rpm) for 1.5 h at 4 °C. The predominant light scattering band located in the lower one-third of the gradient and containing the virions was removed by side puncture of the gradient tube. Approximately 0.3 mL of this solution was mixed with 25 mL of PBS and subjected to centrifugation in a Ti60 fixed-angle rotor at 161,000 × g (40,000 rpm) for 2 h at 4 °C. The final pellet was resuspended overnight in 0.2 to 0.5 mL PBS aliquoted and stored frozen at −80 °C for use in subsequent imaging and infection experiments, without detectable change in infectivity.

Isolation and Propagation of SARS-CoV-2. A human isolate of SARS-CoV-2, Wuhan (B.1), was obtained in accordance with the protocol approved by the Helsinki University Hospital laboratory research permit 30 HUS/32/2018§16. Briefly, a nasopharyngeal swab from a patient infected with COVID19 was suspended in 0.5 mL of universal transport medium (UTM; Copan Diagnostics) and used to inoculate Vero TMPRSS2* cells for 1 h at 37 °C, after which the inoculum was replaced with MEM supplemented with 2% heat-inactivated FBS, L-glutamine, penicillin, and streptomycin, and the virus was allowed to grow for 48 h. Virions in the supernatant (P0) were subjected to a similar second round of propagation (P1) and were analyzed by DNA sequencing, and aliquots were stored at -80 °C in a solution containing MEM, 2% heat-inactivated fetal calf serum, 2 mM L-glutamine, and 1% penicillin-streptomycin. The extent of virus replication was determined by real-time PCR using primers for SARS-CoV-2 RNA-dependent RNA polymerase (40).

VSV-eGFP-SARS-CoV-2 Infection Assays. Infection assays for the Wuhan, Delta, or Omicron VSV-eGFP-SARS-CoV-2 chimeras were done at a final ∼80% confluency of cells plated 1 d before the infection assay as previously described (9) and further explained in *SI Appendix*.

SARS-CoV-2 Infection Assays. All experiments with SARS-CoV-2 were performed in biosafety level 3 facilities at the University of Helsinki with appropriate institutional permits. Virus samples were obtained under Helsinki University Hospital laboratory research permit 30 HUS/32/2018§16. Infections were carried for 16 h at 37 °C with 5% CO_2. Cells were then fixed with 4% paraformaldehyde in PBS for 30 min at room temperature before being processed for immunodetection of viral N protein, automated fluorescence imaging, and image analysis. The detailed protocol is outlined in *SI Appendix*.

VSV-SARS-CoV-2 Atto 565 and Lipid Labeling and Single-Molecule Atto 565 Dye Calibration. Stock solutions of VSV-SARS-CoV-2 and its variants at a concentration of ∼150 μg/mL viral RNA were conjugated with Atto 565-NHS ester (Sigma-Aldrich catalog number 72464) as previously described (41). The number of Atto 565 molecules attached to a single virion was determined by comparing the total fluorescence intensities associated with a given virion and the fluorescence intensity associated with the last bleaching step of the same virion, as previously described (42–44). Lipid labeling of VSV-SARS-CoV-2 Atto 565 was done by brief incubation with Cy5-DOPE (Avanti cat. 810335). A brief description of these steps is outlined in *SI Appendix*.

Trypsin Cleavage of VSV-eGFP-SARS-CoV-2. VSV-eGFP-SARS-CoV-2 and variants (as indicated in text) at a concentration of 30 μg/mL virus RNA in a total volume of 100 μL in DMEM with 25 mM Hepes (pH 7.4) were incubated for 30 min at 37 °C with 1 μg/mL trypsin (Pierce trypsin, TPCK treated from Thermo scientific cat. PI20233). Trypsin activity was terminated with 10 μM aprotinin (bovine lung; Sigma-Aldrich cat. A1153). The required concentration of trypsin was determined by trypsin serial dilution, aiming for the largest infectivity Vero cells whose endogenous cathepsin protease activity had been inhibited with 20 μM E-64 (*SI Appendix*, Fig. S19). Infections were done with VSV or its variants at a concentration of 0.5 μg/mL (for Vero and Vero TMPRSS2) or 5 μg/mL virus RNA (for Caco-2 or Calu-3). When required, the trypsin-cleaved VSVs were used together with infection inhibitors or for pH bypass experiments as described above.

In Vitro Release of S1 from Trypsin-Activated VSV-SARS-CoV-2. VSV-eGFP-SARS-CoV-2-Atto 565 was incubated with trypsin at various concentrations for 30 min, and the reaction was stopped by addition of aprotinin to a final concentration of 10 μM. Virus was then used to infect Vero cells with endogenous cathepsin proteases inhibited with 20 μM E-64 to determine the maximum concentration of trypsin required to proteolytically activate the virus. Virus either without or with trypsin cleavage or with ACE2 bound before and after trypsin cleavage was plated onto a poly-D-lysine–coated glass to determine the number of Atto 565 fluorescence dyes associated with each one of the single particles using spinning-disk confocal microscopy. At least 8,000 particles were imaged per experimental condition to guarantee the ability to distinguish intensity losses of at least 20%. Every experimental condition was repeated in triplicate, and the intensity of the mean intensities of the peak Gaussian fit was used to determine the after and deviation of Atto 565 dyes per condition (*SI Appendix*, Fig. S19).

A computation simulation was performed to validate the ability to detect with statistical significance a 20% fluorescence intensity loss approximately equivalent to the 20 to 30% loss observed in vivo with virions when attached to the cell surface of Vero TMPRSS2. Experimental data corresponding to 8,845 undigested control virions were used to generate a probability density function from which 9 fit parameters (3 mean intensities with corresponding sigmas and the relative contribution to the distribution) were obtained by fitting the sum of 3 Gaussian distributions. These parameters were then used to generate 8,845 random numbers of the same distribution and compared to the experimental data set to illustrate the accuracy of the simulation. A second set of 8,845 random numbers were generated with mean intensities reduced by 20% to generate a probability density distribution representing the fluorescence intensities after ACE2-mediated release of S cleavage by TMPRSS2.

Nasal pH and Temperature Measurements. The pH and temperature of the nasal cavity, close to the inferior surface of the lower turbinate, from each nostril from 17 healthy volunteers, age 26 to 55, males and females, were determined using a Digitrapper pH 400 recorder (Medtronic) connected to a single-use Versaflex disposal dual-sensor pH catheter (Medtronic) and a Beurer FT 15/1digital thermometer (Beurer), respectively. The temperature-dependent pH response of the Digtrapper was corrected to consider the temperature in the nostrils determined for each volunteer.

The full study protocol was approved by the ethical committee of Hospital District of Helsinki and Uusimaa, Finland (HUS/1801/2017; HUS/2502/2020). Written informed consent was received from all subjects.

Preparation of Glass Coverslips. Infection and uptake assays of VSV-eGFP-SARS-CoV-2 and VSV-P-eGFP-SARS-CoV-2 done by spinning-disk confocal microscopy visualization were performed using 25-mm #1.5 coverslips bound with polydimethylsiloxane of about 1 mm in thickness and of 3 mm (infection) or 5 mm (uptake) in diameter wells punched as previously described (9) (*SI Appendix*).

Live-Cell Spinning-Disk Confocal Microscopy. Visualization experiments were done with an inverted spinning-disk confocal microscope (42) following the details described in *SI Appendix*.

LLSM. Cells were plated in a 35-mm culture dish containing 5 mm in diameter glass coverslips to achieve 60% final confluency the day of each experiment. Immediately before lattice light sheet visualization, the coverslip was placed on top of parafilm placed in a 10 cm in diameter Petri dish including wet chem wipes to maintain humidity. A 10 μL solution containing VSV-SARS-CoV-2 in DMEM with 25 mM Hepes at pH 7.4 incubated with cells for the times indicated in the text, after which the coverslips were transferred to the imaging stage of the LLSM. Visualization was done using phenol red–free media, (FluoroBrite) supplemented with 5% FBS and 25 mM Hepes at the indicated pH. Imaging was done at 37 °C in the presence of 5% CO_2 and 100 nM fluorescent Alexa 647 or Alexa 549 dyes added to the medium to determine the cell boundary. The LLSM was operated in sample scan mode with 0.25-μm spacing between each plane along the z-imaging axis and samples imaged as a time series of stacks acquired 1 to 5 s using dithered multi-Bessel lattice light sheet illumination (40, 43). When we used gene-edited SVG-A cells expressing EEA1-Scarlet and NPC1-Halo, Halo was first labeled by incubation of the cells with 200 nM JFX646 for 30 min at 37 °C and 5% CO_2 followed by three 2-min washes with DMEM containing 10% FBS and 25 mM Hepes (pH 7.4) within 2 h prior to virus addition to the coverslip. A time series containing 120 to 300 z-stacks, sequentially obtained every 1 to 5 s, were acquired with ∼10-ms exposures per channel. The time series obtained every 4 s with a 5-ms exposure were used to follow VSV-SARS-CoV-2 Atto 565 labeled with Cy5-DOPE.

The following protocol was used to determine the dwell time between binding of trypsin-activated VSV-SARS-CoV-2-Atto 565 Wuhan and release of the S-fragment. Briefly, trypsin-activated virions at 5 μg/mL viral RNA were flowed on top of Vero cells plated in a homemade microfluidic flow cell 1 d prior to the experiment to achieve a 90% confluency. Soluble 100 nM Alexa 549 added to the medium was used to determine the cell outline. Samples were imaged with an AO-LLSM microscope configured for sample scan imaging to acquire every 4 s a stack with planes separated by 0.3 μm along the z-optical axis using an exposure of 3 ms/plane.

Single-Virus Tracking and Image Analysis. The 3D stacks obtained using LLSM were deskewed and the diffraction limited spots were detected and tracked in three dimensions using the automated detection algorithms that uses least-squares minimization numerical fitting with a model of the microscope point spread function approximated by a 3D Gaussian function and implemented using the MATLAB developed previously (40) available for download (https://github.com/VolkerKirchheim/TrackBrowser_Matlab.git). Estimated fluorescent intensities associated with each spot were calculated from the corresponding amplitudes of the fitted 3D Gaussian and compared to those from single virions bound to poly-D-lysine–coated glass imaged under the same acquisition conditions and whose dye content was determined by single bleaching steps (43).

Tracks with intensities corresponding to a single virus were exported into a custom-made program written in LabView for visualizing trajectories available for download (https://github.com/VolkerKirchheim/TrackBrowser_LabView.git). Each virus trajectory was visually examined for colocalization within a specific compartment (cell surface, EEA1 early endosomes or NPC-1 late endosomes/lysosomes, cytosol) and the MSDs were calculated from all 3D coordinates for all possible time frames within that compartment. A nonlinear relationship between MSD and time for anomalous diffusion was fitted to the MSD data according to the power law in equation:

$$MSD(t) = 6\ K\ t^{\alpha},$$

where K is the generalized diffusion coefficient and α is the anomalous exponent.

Statistical Analysis. An unpaired t test was used to determine the statistical significance in the difference between control and experimental values.

Data, Materials, and Software Availability. All materials and data, including the raw 3D time series acquired with LLSM in this study, are available upon request. Further information and requests for resources and reagents should be directed to and will be fulfilled by the lead contact, Dr. Tom Kirchhausen, kirchhausen@crystal.harvard.edu. The LabView code for visualizing trajectories is available for download (https://github.com/VolkerKirchheim/TrackBrowser_LabView.git) (45). This study did not generate any unique large-scale datasets. Requests for VSV-SARS-CoV-2 chimeras and their material transfer agreements should be directed to and will be fulfilled by Dr. Sean Whelan, spjwhelan@wustl.edu.

ACKNOWLEDGMENTS. We thank Stephen C. Harrison for comments, suggestions, and extensive editorial assistance and members of our laboratories for help and encouragement; the staff at Helsinki University Hospital Diagnostic Center Virology and Immunology for providing human nasal swabs for virus isolation, Suvi Kuivanen and Teemu Smura for virus propagation, sequencing, and discussions, and Sanna Mäki for excellent technical work; E.S. (T.K. laboratory) for excellent laboratory management; Tegy John Vadakkan for maintaining the spinning-disc confocal microscope; Lena Tveriakhina (Blacklow laboratory, Harvard Medical School) for western blot analysis; and Bing Chen for providing soluble ACE2. We appreciate the following: NIH Maximizing Investigators' Research Award (MIRA) GM130386 (T.K.); NIH Grant AI163019 (S.P.J.W. and T.K.); the Danish Technical University (T.K.); Sana Biotechnology (T.K.); Harvard Virology Program, NIH Training Grant T32 AI07245 postdoctoral fellowship (A.J.B.K.); Academy of Finland Research Grant 318434 (G.B. and R.O.); Academy of Finland Research Grant 336490 (O.V.); Helsinki University Hospital Funds TYH2021343 and Jane and Aatos Erkko Foundation (O.V.); and the University of Helsinki Graduate Program in Microbiology and Biotechnology (R.O.); NIH Grant AI030557 (V.K.).

Author affiliations: [a]Department of Cell Biology, Harvard Medical School, Boston, MA 02115; [b]Program in Cellular and Molecular Medicine, Boston Children's Hospital, Boston, MA 02115; [c]Department of Molecular Microbiology, Washington University in Saint Louis, St. Louis, MO 63110; [d]Department of Virology, Faculty of Medicine, University of Helsinki, Helsinki, 00290 Finland; [e]Department of Otorhinolaryngology and Phoniatrics - Head and Neck Surgery, University of Helsinki and Helsinki University Hospital, Helsinki, 00290 Finland; [f]Department of Pharmacology, University of Virginia, Charlottesville, VA 22903; [g]Department of Pediatrics, Harvard Medical School, Boston, MA 02115; [h]Department of Allergy, University of Helsinki and Helsinki University Hospital, Helsinki, 00290 Finland; [i]Center for Membrane and Cell Physiology, University of Virginia, Charlottesville, VA 22903; [j]Department of Molecular Physiology and Biological Physics, University of Virginia, Charlottesville, VA 22903; [k]Department of Veterinary Biosciences, University of Helsinki, Helsinki, 00290 Finland; [l]Virology and Immunology, Helsinki University Hospital Diagnostic Center, Helsinki, 00290 Finland; and [m]The Queensland Brain Institute, University of Queensland, Brisbane, 4072 Australia

1. M. Hoffmann *et al.*, SARS-CoV-2 cell entry depends on ACE2 and TMPRSS2 and is blocked by a clinically proven protease inhibitor. *Cell* **181**, 271–280.e8 (2020).
2. D. Wrapp *et al.*, Cryo-EM structure of the 2019-nCoV spike in the prefusion conformation. *Science* **367**, 1260–1263 (2020).
3. J. Yang *et al.*, Molecular interaction and inhibition of SARS-CoV-2 binding to the ACE2 receptor. *Nat. Commun.* **11**, 4541 (2020).
4. R. Yan *et al.*, Structural basis for the recognition of SARS-CoV-2 by full-length human ACE2. *Science* **367**, 1444–1448 (2020).
5. J. Shang *et al.*, Cell entry mechanisms of SARS-CoV-2. *Proc. Natl. Acad. Sci. U.S.A.* **117**, 11727–11734 (2020).
6. C. B. Jackson, M. Farzan, B. Chen, H. Choe, Mechanisms of SARS-CoV-2 entry into cells. *Nat. Rev. Mol. Cell Biol.* **23**, 3–20 (2022).
7. B. A. Johnson *et al.*, Loss of furin cleavage site attenuates SARS-CoV-2 pathogenesis. *Nature* **591**, 293–299 (2021).
8. R. Zang *et al.*, TMPRSS2 and TMPRSS4 promote SARS-CoV-2 infection of human small intestinal enterocytes. *Sci. Immunol.* **5**, eabc3582 (2020).
9. A. J. B. Kreutzberger *et al.*, Synergistic block of SARS-CoV-2 infection by combined drug inhibition of the host entry factors PIKfyve kinase and TMPRSS2 protease. *J. Virol.* **95**, e0097521 (2021).
10. X. Ou *et al.*, Characterization of spike glycoprotein of SARS-CoV-2 on virus entry and its immune cross-reactivity with SARS-CoV. *Nat. Commun.* **11**, 1620 (2020).
11. T. P. Peacock *et al.*, The furin cleavage site in the SARS-CoV-2 spike protein is required for transmission in ferrets. *Nat. Microbiol.* **6**, 899–909 (2021).
12. D. Bestle *et al.*, TMPRSS2 and furin are both essential for proteolytic activation of SARS-CoV-2 in human airway cells. *Life Sci. Alliance* **3**, e202000786 (2020).

13. J. B. Case *et al.*, Neutralizing antibody and soluble ACE2 inhibition of a replication-competent VSV-SARS-CoV-2 and a clinical isolate of SARS-CoV-2. *Cell Host Microbe* **28**, 475–485.e5 (2020).
14. B.-C. Chen *et al.*, Lattice light-sheet microscopy: Imaging molecules to embryos at high spatiotemporal resolution. *Science* **346**, 1257998 (2014).
15. C. J. Bradish, J. B. Kirkham, The morphology of vesicular stomatitis virus, (Indiana C) derived from chick embryos or cultures of BHK21/13 cells. *Microbiology* **44**, 359–371 (1966).
16. D. K. Cureton, R. H. Massol, S. P. J. Whelan, T. Kirchhausen, The length of vesicular stomatitis virus particles dictates a need for actin assembly during clathrin-dependent endocytosis. *PLoS Pathog.* **6**, e1001127 (2010).
17. J. Klumperman, G. Raposo, The complex ultrastructure of the endolysosomal system. *Cold Spring Harb. Perspect. Biol.* **6**, a016857 (2014).
18. S. M. Ferguson, P. De Camilli, Dynamin, a membrane-remodelling GTPase. *Nat. Rev. Mol. Cell Biol.* **13**, 75–88 (2012).
19. H. Damke, T. Baba, D. E. Warnock, S. L. Schmid, Induction of mutant dynamin specifically blocks endocytic coated vesicle formation. *J. Cell Biol.* **127**, 915–934 (1994).
20. E. Macia *et al.*, Dynasore, a cell-permeable inhibitor of dynamin. *Dev. Cell* **10**, 839–850 (2006).
21. Y.-L. Kang *et al.*, Inhibition of PIKfyve kinase prevents infection by Zaire ebolavirus and SARS-CoV-2. *Proc. Natl. Acad. Sci. U.S.A.* **117**, 20803–20813 (2020).
22. R. Zang *et al.*, Cholesterol 25-hydroxylase suppresses SARS-CoV-2 replication by blocking membrane fusion. *Proc. Natl. Acad. Sci. U.S.A.* **117**, 32105–32113 (2020).
23. S. Belouzard, V. C. Chu, G. R. Whittaker, Activation of the SARS coronavirus spike protein via sequential proteolytic cleavage at two distinct sites. *Proc. Natl. Acad. Sci. U.S.A.* **106**, 5871–5876 (2009).
24. Y. Liu, H.-Q. Qu, J. Qu, L. Tian, H. Hakonarson, Expression pattern of the SARS-CoV-2 entry genes *ACE2* and *TMPRSS2* in the respiratory tract. *Viruses* **12**, 1174 (2020).
25. S. P. Sajuthi *et al.*, Type 2 and interferon inflammation regulate SARS-CoV-2 entry factor expression in the airway epithelium. *Nat. Commun.* **11**, 5139 (2020).
26. R. J. A. England, J. J. Homer, L. C. Knight, S. R. Ell, Nasal pH measurement: A reliable and repeatable parameter. *Clin. Otolaryngol. Allied Sci.* **24**, 67–68 (1999).
27. B.-G. Kim *et al.*, Nasal pH in patients with chronic rhinosinusitis before and after endoscopic sinus surgery. *Am. J. Otolaryngol.* **34**, 505–507 (2013).
28. I. Glowacka *et al.*, Evidence that TMPRSS2 activates the severe acute respiratory syndrome coronavirus spike protein for membrane fusion and reduces viral control by the humoral immune response. *J. Virol.* **85**, 4122–4134 (2011).
29. G. Simmons *et al.*, Different host cell proteases activate the SARS-coronavirus spike-protein for cell-cell and virus-cell fusion. *Virology* **413**, 265–274 (2011).
30. J. K. Millet, G. R. Whittaker, Host cell entry of Middle East respiratory syndrome coronavirus after two-step, furin-mediated activation of the spike protein. *Proc. Natl. Acad. Sci. U.S.A.* **111**, 15214–15219 (2014).
31. D. L. Floyd, J. R. Ragains, J. J. Skehel, S. C. Harrison, A. M. van Oijen, Single-particle kinetics of influenza virus membrane fusion. *Proc. Natl. Acad. Sci. U.S.A.* **105**, 15382–15387 (2008).
32. T. Ivanovic, J. L. Choi, S. P. Whelan, A. M. van Oijen, S. C. Harrison, Influenza-virus membrane fusion by cooperative fold-back of stochastically induced hemagglutinin intermediates. *eLife* **2**, e00333 (2013).
33. L. H. Chao, D. E. Klein, A. G. Schmidt, J. M. Peña, S. C. Harrison, Sequential conformational rearrangements in flavivirus membrane fusion. *eLife* **3**, e04389 (2014).
34. I. S. Kim *et al.*, Mechanism of membrane fusion induced by vesicular stomatitis virus G protein. *Proc. Natl. Acad. Sci. U.S.A.* **114**, E28–E36 (2017).
35. B. Meng *et al.*; CITIID-NIHR BioResource COVID-19 Collaboration; Genotype to Phenotype Japan (G2P-Japan) Consortium; Ecuador-COVID19 Consortium, Altered TMPRSS2 usage by SARS-CoV-2 Omicron impacts infectivity and fusogenicity. *Nature* **603**, 706–714 (2022).
36. H. Zhao *et al.*, SARS-CoV-2 Omicron variant shows less efficient replication and fusion activity when compared with Delta variant in TMPRSS2-expressed cells. *Emerg. Microbes Infect.* **11**, 277–283 (2022).
37. D. Bojkova *et al.*, Reduced interferon antagonism but similar drug sensitivity in Omicron variant compared to Delta variant of SARS-CoV-2 isolates. *Cell Res.* **32**, 319–321 (2022).
38. R. M. Effros, F. P. Chinard, The in vivo pH of the extravascular space of the lung. *J. Clin. Invest.* **48**, 1983–1996 (1969).
39. R. D. de Vries *et al.*, Intranasal fusion inhibitory lipopeptide prevents direct-contact SARS-CoV-2 transmission in ferrets. *Science* **371**, 1379–1382 (2021).
40. F. Aguet *et al.*, Membrane dynamics of dividing cells imaged by lattice light-sheet microscopy. *Mol. Biol. Cell* **27**, 3418–3435 (2016).
41. A. H. Abdelhakim *et al.*, Structural correlates of rotavirus cell entry. *PLoS Pathog.* **10**, e1004355 (2014).
42. E. Cocucci, F. Aguet, S. Boulant, T. Kirchhausen, The first five seconds in the life of a clathrin-coated pit. *Cell* **150**, 495–507 (2012).
43. Y.-Y. Chou *et al.*, Inherited nuclear pore substructures template post-mitotic pore assembly. *Dev. Cell* **56**, 1786–1803.e9 (2021).
44. Y. Chen, N. C. Deffenbaugh, C. T. Anderson, W. O. Hancock, Molecular counting by photobleaching in protein complexes with many subunits: Best practices and application to the cellulose synthesis complex. *Mol. Biol. Cell* **25**, 3630–3642 (2014).
45. V. Kirchheim, TrackBrowser_LabView. GitHub. https://github.com/VolkerKirchheim/TrackBrowser_LabView.git. Deposited 23 May 2022.